ARTICLE

Inclusion boundary reconstruction and sensitivity analysis in Electrical Impedance Tomography

Shangjie Ren[a], Manuchehr Soleimani[b], Yaoyuan Xu[c,b], Feng Dong[a]

[a]Tianjin Key Laboratory of Process Measurement and Control, School of Electrical and Information Engineering, Tianjin University, Tianjin, 300072, China;
[b]Engineering Tomography Laboratory (ETL), Department of Electronic and Electrical Engineering, University of Bath, Bath, BA2 7AY, UK;
[c]Province-Ministry Joint Key Laboratory of Electromagnetic Field and Electrical Apparatus Reliability, Hebei University of Technology, Tianjin, 300401, China.

ARTICLE HISTORY
Compiled September 6, 2017

ABSTRACT
Reconstruction of conductive inclusions in a homogeneous background medium is commonly seen in EIT. One of the methods to deal with the inclusion reconstruction problems is the shape-based method. With prior knowledge of conductivity of target inclusions, the boundary of inclusions is parameterized by several shape coefficients and recovered from EIT measurements. This paper presents a shape-based inclusion reconstruction method and its numerical implementation with Boundary Element Method (BEM). A Shape Perturbation Method (SPM) is proposed to calculate the shape sensitivity in EIT. To evaluate the accuracy of the presented method, a series of numerical tests are conducted. The characteristics of EIT shape sensitivity are analyzed. Some factors influencing the reconstruction performance are discussed.

KEYWORDS
Inverse problem, electrical impedance tomography; inclusion reconstruction; shape sensitivity; boundary element method.

1. Introduction

Electrical Impedance Tomography (EIT) is a non-invasive technique to image the conductivity within an observation domain from the measurements on its boundary. One of the commonly seen applications of EIT is to reconstruct the inclusions in a homogeneous background medium, e.g. detecting tumor [1, 2], monitoring respiratory process [3, 4], imaging air bubbles in liquids [5, 6]. With prior knowledge of the conductivity values of the inclusions, the boundary of the inclusions can be parameterized by a set of shape coefficients, then reconstructed from EIT measurements. Since the boundary reconstruction results can be directly used for quantitative analysis, this kind of shape-based inclusion boundary reconstructions has been widely studied, e.g. Haddar and Kress [7] employed a conformal mapping technique to reconstruct a perfectly conducting inclusion from Cauchy data, Cakoni and Kress [8] determined the shape of an inclusion by using the method of boundary integral equations, Soleimanis et al. [9]

CONTACT Feng Dong. Email: fdong@tju.edu.cn

utilized level sets method to enhance the resolution at the inclusion boundary, Dyhoum et al. [10] presented a method to reconstruct the rigid inclusions in the Complete Electrode Model (CEM) [11] of ERT.

This paper focuses on the numerical implementation of the inclusion boundary reconstruction method with Boundary Element Method (BEM). Comparing with more widely used Finite Element Method (FEM), BEM mainly owns two advantages for the boundary reconstructions. Firstly, the discretization in BEM is only over the boundary. This simplifies the numerical modeling of the target inclusions, and reduce the number of unknowns by one order. Secondly, BEM is effective for accurately computing the field variables at the boundary, which is important for keeping the accuracy of the boundary reconstruction. Duraiswami et al. [12] utilized BEM to solve the EIT problem. In their method, the boundary of inclusions was parameterized with Legendre polynomials and recovered by using the output least squares approach. Latter, Babaeizadeh and Brooks [13] extended this BEM to reconstruct a 3D inclusion parameterized by spherical harmonics. Xu et al. [14] derived an analytical boundary element integral method for solving the inclusion problems with more accuracy. Tan et al. [15] used the analytical boundary element integral method to determine the 2D inclusion boundary from experimental data. Recently, Ren et al. [16] reconstructed the boundary of a 3D inclusion with cubic Electrical Capacitance Tomography (ECT) sensor. However, in previous reports, there was a lack of formal derivation of shape sensitivity formula for the CEM of EIT. For example, the direct linear method in [13] is for 3D EIT with shunting electrode model, the analytical method in [14] is for 2D EIT problems, the shape derivative in [16] is for 3D ECT problems with start-shaped inclusion. Moreover, the previous reports mainly focus on the reconstruction of a single inclusion or multiple inclusions with same conductivity.

In this paper, a inclusion boundary reconstruction method and its numerical implementation with BEM are presented. A boundary integral formula is derived for calculating the shape sensitivity for the CEM of EIT. The derivation is by using the Shape Perturbation Method (SPM), and is efficient in both 2D and 3D. A series of numerical tests are conducted to evaluate the accuracy of the presented methods. The influence of decisive factors, such as: the shape of the boundary, the position of the inclusion, and the conductivity contrast between the inclusion and background medium, on the EIT shape sensitivity are discussed.

2. Methodology

2.1. *Direct problem*

As it is shown in Figure 1, the observation bounded domain Ω is with a smooth boundary $\partial\Omega$. According to Maxwell's equations and quasi-static assumption, the electric potential u is governed by the elliptic partial differential equation

$$\nabla \cdot (\sigma(\mathbf{x})\nabla u(\mathbf{x})) = 0, \quad \mathbf{x} \in \Omega, \tag{1}$$

where $\mathbf{x} \in \mathbb{R}^d$ is the spatial variable in d dimensions, and $\sigma(\mathbf{x}) > 0$ is the conductivity at Ω. In practical EIT system, a series of electrodes are fixed at the peripheral of the observation domain. Electric currents are supplied at some of the electrodes, while constant voltage responses at the rest electrodes are collected. The associated

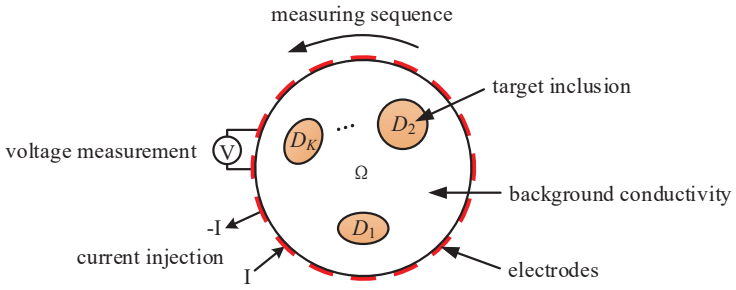

Figure 1. A 2D illustration of inclusion recovery problems in EIT.

boundary conditions are formalized in the CEM

$$\begin{aligned} \int_{E_l} \sigma(\mathbf{x})q(\mathbf{x})\mathrm{d}S &= I_l, \quad \mathbf{x} \in E_l,\ l = 1, 2, \ldots, L, \\ u(\mathbf{x}) + z_l\sigma(\mathbf{x})q(\mathbf{x}) &= V_l, \quad \mathbf{x} \in E_l,\ l = 1, 2, \ldots, L, \\ \sigma(\mathbf{x})q(\mathbf{x}) &= 0, \quad \mathbf{x} \in G, \end{aligned} \tag{2}$$

where $q = \nabla u \cdot \nu$, ν is the outward unit normal at the counterclockwise oriented boundary $\partial\Omega$, z_l is the contact impedance between the l-th electrode and the background medium, $E_l \subset \partial\Omega$ is the l-th electrode, L is the total number of the electrodes, $G = \partial\Omega \backslash \cup_{l=1}^{L} E_l$ is the collection of the inter-electrodes gaps, I_l and V_l are the electrode current and constant voltage, respectively.

For a given vector of electrode currents $\mathbf{I} = [I_1, I_2, \ldots, I_L]^T$ and a known conductivity $\sigma(\mathbf{x})$, the electrode voltages $\mathbf{V} = [V_1, V_2, \ldots, V_L]^T$ can be calculated by solving the boundary value problem defined by (1) and (2). Due to the limited voltage rejection ratio of electronic circuit, a large common voltage may reduce the measurement sensitivity. Consequently, the electrode voltage drops, which are much smaller than the electrode voltages, are taken as measurements. For example, the Sheffield system [17] takes the voltage drops between the adjacent electrodes as the measurements. Correspondingly, the EIT measurements are collected by

$$U^{\mathbf{I},\mathbf{M}} = \mathbf{M}^T\mathbf{V}^{\mathbf{I}}(\sigma), \tag{3}$$

where $\mathbf{M} \in \mathbb{R}^{L\times 1}$ is the voltage collection pattern, $\mathbf{I} \in \mathbb{R}^{L\times 1}$ is the current supply pattern, and $\mathbf{V}^{\mathbf{I}}(\sigma)$ is used to emphasize the dependence of electrode voltages on the conductivity and the current supply pattern.

Geometric configuration of the inclusion reconstruction problem is shown in Figure 1. The observation domain is divided into a finite number of sub-regions

$$\Omega = \cup_{k=0}^{K} D_k \quad \text{and} \quad D_k \cap D_{k'} = \emptyset \text{ for } k \neq k', \tag{4}$$

where D_0 is the multi-connected sub-region occupied by the background medium, D_k, for $k \geq 1$, is the simply-connected sub-region occupied by the k-th inclusion, and K is the total number of inclusions. The inclusion sub-region D_k and background medium sub-region D_0 share the smooth enough boundary (interior boundary) Γ_k. The exterior (outmost) boundary of observation domain Ω is denoted with $\partial\Omega = \Gamma_0$. The boundary of background sub-region D_0 follows $\partial D_0 = \cup_{k=0}^{K}\Gamma_k$. The conductivity

at each sub-region is constant and satisfies

$$\sigma(\mathbf{x}) = \begin{cases} \sigma_0, & \mathbf{x} \in D_0, \\ \sigma_k, & \mathbf{x} \in D_k,\ k = 1, 2, \ldots, K, \end{cases} \tag{5}$$

where σ_0 is background conductivity, and σ_k is conductivity of the k-th inclusion, $\sigma_k \neq \sigma_0$ implies that the conductivity is discontinuous at Γ_k.

If the outmost boundary Γ_0 is given, with prior knowledge of the conductivity values $\mathbf{\Sigma} = [\sigma_0, \sigma_1, \cdots, \sigma_K]$, the conductivity distribution $\sigma(\mathbf{x})$ at the entire observation domain $\Omega = \cup_{k=0}^{K}$ is uniquely determined by the inclusion boundaries $\mathbf{\Gamma} = [\Gamma_1, \Gamma_2, \cdots, \Gamma_K]$. Correspondingly, the direct problem is to compute the EIT measurements $\mathbf{U}$ from given inclusion boundaries $\mathbf{\Gamma}$, while the inverse problem is to reconstruct the inclusion boundaries $\mathbf{\Gamma}$ from given measurements $\mathbf{U}$.

2.2. *Inverse problem*

Without loss of generality, a more general inverse problem is considered. The boundary $\mathbf{\Gamma}$ and conductivity $\mathbf{\Sigma}$ of the inclusions are both unknown, and required to be reconstructed from the measurements $\mathbf{U}$. This problem is ill-posed and non-linear. To obtain a stable solution, a regularized output least squares method is suggested. The unknown inclusion boundary and conductivity are estimated by minimizing the following least squares function

$$\|\mathbf{U}(\mathbf{\Gamma}, \mathbf{\Sigma}) - \mathbf{U}^*\|^2 + \lambda_{\mathbf{\Gamma}} \|\mathbf{\Gamma} - \mathbf{\Gamma}^0\|^2 + \lambda_{\mathbf{\Sigma}} \|\mathbf{\Sigma} - \mathbf{\Sigma}^0\|^2, \tag{6}$$

where λ_Γ and λ_Σ are regularization parameters, $\|\cdot\|$ is the Euclidean norm, $\mathbf{U}^*$ represents the physical measurements, $\mathbf{\Gamma}^0$ and $\mathbf{\Sigma}^0$ are the prior guesses of Γ and Σ, respectively. The last two terms in (6) are boundary and conductivity regularization terms preventing the solutions from too different from the prior knowledge.

It is worth to notice that the EIT measurement changes caused by the inclusion boundary perturbation are significantly different from the measurement changes caused by the inclusion conductivity perturbation. Consequently, it is difficult to reconstruct Γ and Σ at the same time. As an alternative, an alternating minimization schedule is preferred. The unknown variables are partitioned into the 'inclusion boundary' block and 'inclusion conductivity' block. Each block of variables is alternatively updated by minimizing the regularized least squares function (6) with respect to one block at a time while the other block is fixed. This kind of group updating strategy has the advantage of incorporating different kinds of prior constraints for different kinds of target variables, and thus improves the reconstruction performance. The separated boundary or conductivity reconstruction problem, as a sub-problem from (6) can be solved by Newton's method. As described in [18], the shape Hessian at the global minimizer is not coercive, which means that the Newton-kind minimizer may not be a local strict minimum of the criterion. Fortunately, the numerical [14] and experimental results [15, 16] show that, after starting from a good initial guess, the Newton-type shape reconstruction method performs well at least for reconstructing simple shaped inclusions.

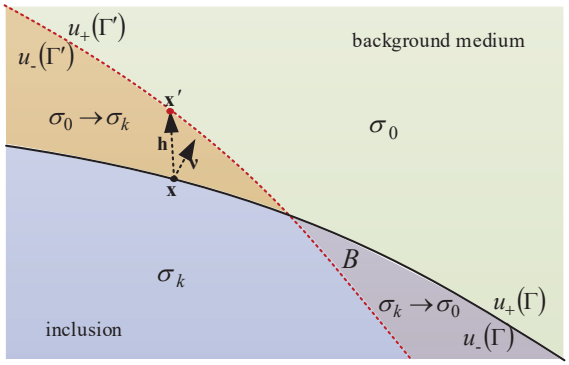

Figure 2. Conductivity and shape changes caused by the interface perturbation.

2.3. *Shape sensitivity formula*

In Newton's solution of (6), it is necessary to evaluate the derivatives of $\mathbf{U}$ with respect to the target variables $\mathbf{\Gamma}$ or $\mathbf{\Sigma}$. In this subsection, a Boundary Integral Equation (BIE) is derived to evaluate the shape sensitivity. The numerical implementation of the presented shape sensitivity formula will be described in the next section.

As it is shown in Figure 2, the target inclusion has deformed from D_k to D_k'. The inclusion boundary is correspondingly changed from Γ_k to Γ_k'. This process can be mathematically interpreted by the motion of virtual mass points. Assuming a set of mass points $\mathbf{x} \in \Gamma_k$ at the original boundary, the boundary changes imply the mass points $\mathbf{x}$ passing through a displacement $\mathbf{h}$ to new locations $\mathbf{x}' = \mathbf{x} + \mathbf{h}(\mathbf{x}) \in \Gamma_k'$ at the deformed boundary. If the displacement is sufficiently smooth, the inclusion deformation is preserved. Starting from this point, the conductivity perturbation caused by the inclusion deformation follows

$$\delta\sigma(\mathbf{x}) = \begin{cases} sgn(h)(\sigma_k - \sigma_0), & \mathbf{x} \in B, \\ 0, & \mathbf{x} \in \Omega \backslash B, \end{cases} \tag{7}$$

where $h = \mathbf{h} \cdot \nu$ is the component of displacement at the outward normal direction, $sgn(\cdot)$ is the signum function, and $B = (D_k \cup D_k') \backslash (D_k \cap D_k')$ is the symmetric difference of the original and deformed inclusions. Positive displacements imply the inclusion boundary moving toward the background medium side, while negative displacements imply the inclusion boundary moving toward the inclusion side.

The electrical fields at the sides of background medium and inclusion are denoted with ∇u_+ and ∇u_-, respectively. Substituting (7) into (39) in appendix section, the voltage measurement change caused by the inclusion boundary perturbation is

$$\delta U^{\mathbf{I},\mathbf{M}} = (\sigma_0 - \sigma_k) \int_B sgn(h) \nabla u^{\mathbf{I}}_{+sgn(h)}(\Gamma_k) \cdot \nabla u^{\mathbf{M}}_{-sgn(h)}(\Gamma_k') \mathrm{d}V, \tag{8}$$

where $u^{\mathbf{I}}(\Gamma_k)$ is the electric potential from current pattern $\mathbf{I}$ with unchanged inclusion boundary Γ_k, and $u^{\mathbf{M}}(\Gamma_k')$ is the electric potential from current pattern $\mathbf{M}$ with changed inclusion boundary Γ_k'. Different from (3), the measurement pattern $\mathbf{M}$, which has the same scale with the current pattern $\mathbf{I}$, is used as the current pattern.

Direct calculation of the volume integral equation (8) is possible, but complicated and time-consuming, especially in the problems of reconstructing irregularly-shaped

inclusions. If the displacement $\mathbf{h}$ is sufficiently small, the infinitesimal volume element forming B can be approximated by $\mathrm{d}V = \mathrm{d}\mathbf{h}\cdot\mathrm{d}\mathbf{S}$. An boundary integral approximation of (8) is then derived as

$$\delta U^{\mathbf{I},\mathbf{M}} = (\sigma_0 - \sigma_k) \int_{\Gamma_k} h \nabla u^{\mathbf{I}}_{+sgn(h)} (\Gamma_k) \cdot \nabla u^{\mathbf{M}}_{-sgn(h)} \left(\Gamma'_k\right) \mathrm{d}S. \tag{9}$$

According to electromagnetic theory, $\sigma_0 \nabla u_+(\Gamma_k) = \sigma_k \nabla u_-(\Gamma_k)$ at Γ_k, the electric current density is continuous at the inclusion boundary. Consequently, the dot product of the electric fields in (9) satisfies

$$\nabla u^{\mathbf{I}}_{+sgn(h)} \cdot \nabla u^{\mathbf{M}}_{-sgn(h)} = \nabla u^{\mathbf{I}}_{+} \cdot \nabla u^{\mathbf{M}}_{-} = \nabla u^{\mathbf{I}}_{-} \cdot \nabla u^{\mathbf{M}}_{+}. \tag{10}$$

Since the boundary displacement is small enough, the electric potential $u(\Gamma'_k)$ can be approximated by $u(\Gamma_k) + \delta u$. Applying this approximation and (10) on (8), then ignoring the high order terms in the result, a boundary integral formula for shape sensitivity calculation is derived as

$$\delta U^{\mathbf{I},\mathbf{M}} = (\sigma_0 - \sigma_k) \int_{\Gamma_k} \left(\kappa_k q^{\mathbf{I}} q^{\mathbf{M}} + \nabla_{\parallel} u^{\mathbf{I}} \nabla_{\parallel} u^{\mathbf{M}}\right). \tag{11}$$

where $\kappa_k = \sigma_k/\sigma_0$ is the conductivity contrast between the k-th inclusion and the background medium, $\nabla_{\parallel}$ is the differential operator at the tangential direction of the boundary, $u = u_+$ and $q = q_+$ are the potential and flux at the side of background medium. According to (11), the power perturbation caused by a small deformation of the inclusion boundary is mainly dissipated at the small neighborhood around this boundary. In the next section, different inferences of (11) are numerically implemented with BEM.

3. Numerical Implementation

In this section, the BEM formulation of EIT direct problem with CEM is presented, then the shape and conductivity derivatives are evaluated in the framework of BEM.

3.1. *Boundary element method*

According to (4) and (5), the domain Ω consists of a finite number of sub-regions D_k. Consequently, the governing equation (1) in D_k simplifies as Laplace's equation

$$\triangle u_k(\mathbf{x}) = 0, \quad \mathbf{x} \in D_k,\ k = 0, 1, \ldots, K, \tag{12}$$

where u_k is the electric potential in the k-th sub-region. Applying Green-Gauss's theorem, the potential on ∂D_k satisfies

$$\alpha_k(\mathbf{x}) u_k(\mathbf{x}) + \int_{\partial D_k} u_k(\mathbf{y}) q^*(\mathbf{y},\mathbf{x}) \mathrm{d}S = \int_{\partial D_k} q_k(\mathbf{y}) u^*(\mathbf{y},\mathbf{x}) \mathrm{d}S, \quad \mathbf{x} \in \partial D_k, \tag{13}$$

where u^* is the fundamental solution for Laplace's equation [19], $q^* = \nabla u^* \cdot \nu$ is the outer normal derivative of u^* at the counterclockwise oriented boundary ∂D_k, α is the

geometric coefficient and $\alpha = 0.5$ for smooth enough boundary, $\mathbf{x}$ and $\mathbf{y}$ are commonly referred as the source and field points, respectively.

Solving the BIE (13) requires the boundary conditions at both exterior and interior boundaries. The electric potential and flux at exterior boundary Γ_0 satisfy (2). The electric potential and flux at interior boundary Γ_k, for $k \geq 1$, satisfy the transmission conditions

$$u_0(\mathbf{x}) = u_k(\mathbf{x}) \quad \text{and} \quad q_0(\mathbf{x}) = -\kappa_k q_k(\mathbf{x}), \quad \mathbf{x} \in \Gamma_k, \ k = 1, 2, \ldots, K. \tag{14}$$

Substituting conditions (2) and (14) into (13), the integral equation at the boundary of the background sub-region is given by

$$\begin{aligned} \alpha_0 u_0 \quad &+ \quad \int_G u_0 q^* \mathrm{d}S + \sum_{l=1}^{L} \int_{E_l} u_0 \left(q^* + \frac{z_l u^*}{\sigma_0} \right) \mathrm{d}S - \sum_{l=1}^{L} \frac{z_l V_l}{\sigma_0} \int_{E_l} u^* \mathrm{d}S \\ &- \quad \sum_{k=1}^{K} \int_{\Gamma_k} u_k q^* \mathrm{d}S - \sum_{k=1}^{K} \kappa_k \int_{\Gamma_k} q_k u^* \mathrm{d}S = 0, \end{aligned} \tag{15}$$

where the exterior boundary Γ_0 is further divided into the electrodes part E and the inter-electrode gaps part G. The last two minus signs in (15) are due to the inclusion boundary where being counterclockwise oriented. To save the computational resources, the fluxes q_k can be eliminated by applying (13) into (15), as it was described in [14] for reconstructing perfect conducting inclusions. In the presented inclusion boundary reconstruction where method, this kind of variable elimination method is not suggested. The flux q is necessary in the shape derivative calculation.

Numerically solution of the integral equations (13) and (15) needs the discretization of boundary $\mathbf{\Gamma}$. For simplification, the method of constant boundary elements is used as an example. The boundary Γ_k is divided into a finite number of boundary elements $\triangle\Gamma_k^i$, e.g. line segments in 2D or triangles in 3D. One point $\mathbf{x}_k^i$ (collocation point) is placed at the center of each element $\triangle\Gamma_k^i$. The number of collocation points equals to the number of boundary elements. The electric potential and flux are constant over each boundary element, and are approximated by

$$u_k(\mathbf{x}) = u_k^i \quad \text{and} \quad q_k(\mathbf{x}) = q_k^i \quad \text{for } \mathbf{x} \in \triangle\Gamma_k^i, \tag{16}$$

where u_k^i and q_k^i are the values of u_k and q_k at $\mathbf{x}_k^i$.

Successively choosing the collocation points as the source points, and applying (16) on (13), the discretized integral equation at the boundary of the k-th inclusion yields

$$\sum_{j=1}^{N_k} \mathbf{F}_{k,ij} u_k^j + \sum_{j=1}^{N_k} \mathbf{P}_{k,ij} q_k^j = 0 \quad \text{for } k = 1, 2, \ldots, K, \tag{17}$$

where N_k is the total number of collocation points at the k-th inclusion boundary. Similarly, applying (16) on (15), the discretized integral equation at the boundary of

background medium yields

$$\begin{aligned}\sum_{j=1}^{N_G}\mathbf{F}_{G,ij}u_G^j &+ \sum_{j=1}^{N_E}[\mathbf{F}_{E,ij}+\frac{z_l}{\sigma_0}\mathbf{P}_{E,ij}]u_E^j+\sum_{k=1}^{K}\sum_{j=1}^{N_k}\mathbf{F}_{k,ij}u_k^j \\ &+ \sum_{k=1}^{K}\sum_{j=1}^{N_k}\kappa_k\mathbf{P}_{k,ij}q_k^j+\sum_{l=1}^{L}\mathbf{H}_{il}V_l=0, \end{aligned} \tag{18}$$

where the exterior boundary elements $\triangle\Gamma_0=\triangle\partial\Omega$ is further divided into the inter-electrodes gaps part $\triangle\Gamma_G$ and the electrodes part $\triangle\Gamma_E$, N_G and N_E are the total numbers of boundary elements at $\triangle\Gamma_G$ and $\triangle\Gamma_E$, respectively.

The coefficients, $\mathbf{F}$ and $\mathbf{P}$, in (17) and (18) imply the interactions between the source and field points. The subscripts G, E, and k denote the coefficients calculated at $\triangle\Gamma_G$, $\triangle\Gamma_E$, and $\triangle\Gamma_k$, respectively. For example, the coefficients at Γ_k are given by

$$\mathbf{P}_{k,ij}=\int_{\triangle\Gamma_k^j(\mathbf{y})}q^*(\mathbf{x}^i,\mathbf{y})\mathrm{d}S \quad\text{and}\quad \mathbf{F}_{k,ij}=\frac{1}{2}\delta_{\triangle\Gamma_k^j}(\mathbf{x}^i)+\int_{\triangle\Gamma_k^j(\mathbf{y})}u^*(\mathbf{x}^i,\mathbf{y})\mathrm{d}S, \tag{19}$$

where $\delta_{\triangle\Gamma_k^j}(\mathbf{x}^i)$ is Kronecker delta and $\delta=1$ if and only if $\mathbf{x}^i\in\triangle\Gamma_k^j$. The coefficients $\mathbf{H}$ in (18) are given by

$$\mathbf{H}_{il}=\frac{z_l}{\sigma_0}\sum_{k=1}^{N_{E,l}}\int_{\triangle\Gamma_{E,l}^j(\mathbf{y})}u^*(\mathbf{x}^i,\mathbf{y})\mathrm{d}S, \tag{20}$$

where $\triangle\Gamma_{E,l}$ denotes the boundary elements at the l-th electrode, $N_{E,l}$ is the total number of boundary elements at the l-th electrode.

To evaluate the electrode voltages V from (17) and (18), the electrode current condition is necessary. According to the currents conservation condition $\sum_{l=1}^{L}I_l=0$, the electrode current condition in (2) is rearranged as

$$\frac{1}{z_l}\int_{E_l}(V_l-u_0)\mathrm{d}S-\frac{1}{z_L}\int_{E_L}(V_L-u_0)\mathrm{d}S=I_l-I_L,\quad l=1,2,\ldots,L-1. \tag{21}$$

Applying (16) on (21), the discretized electrode current condition is

$$\sum_{j=1}^{N_{E,l}}\mathbf{C}_{lj}u_{E,l}^j-\sum_{j=1}^{N_{E,L}}\mathbf{C}_{Lj}u_{E,L}^j+\mathbf{D}_lV_l-\mathbf{D}_LV_L=I_l-I_L,\quad l=1,2,\ldots,L-1. \tag{22}$$

where

$$\mathbf{C}_{lj}=\frac{1}{z_l}\int_{\triangle\Gamma_{E,l}^j}\mathrm{d}S=\frac{|\triangle\Gamma_{E,l}^j|}{z_l}\quad\text{and}\quad\mathbf{D}_l=\frac{|E_l|}{z_l}, \tag{23}$$

where $|\triangle\Gamma|$ is the length/area of the boundary element $\triangle\Gamma$.

Combining (17), (18) and (22) together, the system equations become

$$\begin{bmatrix} \mathbf{F}_G & \mathbf{F}_E + \frac{z_l}{\sigma_0}\mathbf{P}_E & \mathbf{F}_1 & \kappa_1\mathbf{P}_1 & \dots & \mathbf{F}_K & \kappa_K\mathbf{P}_K & \mathbf{H} \\ \mathbf{0} & \mathbf{0} & \mathbf{F}_1 & \mathbf{P}_1 & \dots & \mathbf{0} & \mathbf{0} & \mathbf{0} \\ \vdots & \vdots & \vdots & \vdots & \ddots & \vdots & \vdots & \vdots \\ \mathbf{0} & \mathbf{0} & \mathbf{0} & \mathbf{0} & \dots & \mathbf{F}_K & \mathbf{P}_K & \mathbf{0} \\ \mathbf{0} & \mathbf{C} & \mathbf{0} & \mathbf{0} & \mathbf{0} & \dots & \mathbf{0} & \mathbf{D} \\ \mathbf{0} & \mathbf{0} & \mathbf{0} & \mathbf{0} & \mathbf{0} & \dots & \mathbf{0} & \mathbf{E} \end{bmatrix} \begin{bmatrix} \mathbf{u}_G \\ \mathbf{u}_E \\ \mathbf{u}_1 \\ \mathbf{q}_1 \\ \vdots \\ \mathbf{u}_K \\ \mathbf{q}_K \\ \mathbf{V} \end{bmatrix} = \begin{bmatrix} \mathbf{0} \\ \tilde{\mathbf{I}} \\ 0 \end{bmatrix}, \quad (24)$$

where $\tilde{\mathbf{I}} = [I_1 - I_L, \dots, I_{L-1} - I_L]^T$, $\mathbf{E}$ is a $1 \times L$ identity matrix and is derived from the conservation condition $\sum_{l=1}^{L} V_l = 0$. Then (24) is a $(N+L) \times (N+L)$ linear system, N is the total number of boundary elements. Since the variables in (24) are only on the boundary, the BEM system has much smaller scale than the FEM system for solving the same scale EIT direct problem. The non-boundary variables, e.g. electric potentials within the inclusions, are non-essential in the shape-based inclusion boundary and/or conductivity reconstruction.

Another point needed to be mentioned is that the system matrix in (21) is dense and non-symmetric. As a result, $O(N^2)$ operations are required to compute the coefficients and another $O(N^2)$ operations are required to solve the algebraic system of equation (24). This makes the BEM less efficient than FEM for solving large scale EIT problems, e.g. 3D inclusion reconstruction problems with more than hundreds of thousands of boundary elements. By noticing that the exterior boundary Γ_0 is normally given, the coefficients on Γ_0 can be pre-calculated and stored for the iterative reconstruction. This kind of pre-processing technique can save nearly half of the CPU time costed for the coefficients calculation.

3.2. *Shape sensitivity calculation*

The numerical implementation of shape derivative formula (11) depends on the parametrization of the target boundary. One of the most commonly used methods to parameterize a closed boundary is decomposing the boundary with a set of orthogonal functions, e.g. Fourier functions [20] or spherical harmonics [16]. The decomposed boundary is denoted as $\Gamma(t) = \sum \gamma_n s_n(t)$, where t is the local parameter of the target boundary, $s_n(t)$ is the shape basis, and γ_n is the weight of shape basis. The weights γ are treated as unknowns (referred as shape coefficients), and are recovered from the EIT measurements by using (6). According to (11), the derivative of the EIT measurement with respect to the shape coefficient γ_n is

$$\frac{\partial U^{\mathbf{I},\mathbf{M}}}{\partial \gamma_n} = (\sigma_0 - \sigma_k) \int_{\Gamma(t)} s_n \left(\kappa_k q^{\mathbf{I}} q^{\mathbf{M}} + \nabla_{\parallel} u^{\mathbf{I}} \nabla_{\parallel} u^{\mathbf{M}} \right) \mathrm{d}t. \quad (25)$$

Another commonly used method to parameterize a closed boundary is by using the geometric vertices in boundary element meshes. In two dimensional inclusion reconstructions, the boundary of inclusion is divided into a set of line segments. Displacement of a vertex will affect the boundary elements attached with this vertex. As it is shown in Figure 3, the boundary elements (counterclockwise oriented) attached with a given vertex $\mathbf{v}_n$ are denoted by $\triangle\Gamma_k^{n-1} = |\mathbf{v}_n - \mathbf{v}_{n-1}|$ and $\triangle\Gamma_k^{n} = |\mathbf{v}_{n+1} - \mathbf{v}_n|$. The

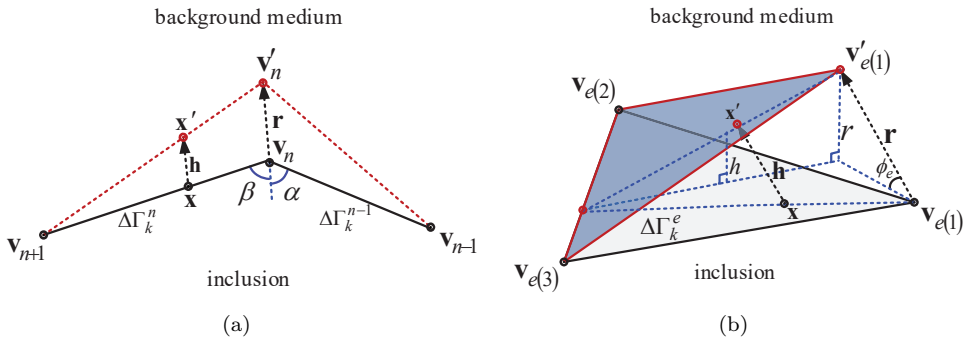

Figure 3. Inclusion boundary deformation caused by vertex perturbation in (a) two dimensions and (b) three dimensions.

vertex displacement is denoted by $\mathbf{r} = \mathbf{v}_n - \mathbf{v}'_n$, where $\mathbf{v}'_n$ is the location of the moved vertex. Correspondingly, the boundary deformation caused by the two dimensional vertex displacement $\mathbf{r}$ satisfies

$$h(t)|_{\triangle\Gamma_k^{n-1}} = r\sin(\alpha)\frac{1+t}{2} \quad \text{and} \quad h(t)|_{\triangle\Gamma_k^{n}} = r\sin(\beta)\frac{1-t}{2}, \tag{26}$$

where $r = |\mathbf{r}|$ is the scalar displacement, $t \in [-1, 1]$ is the local coordinate at the segment $\triangle\Gamma_k^n$, and α and β denotes the angles between the displacement vector $\mathbf{r}$ and the boundary elements $\triangle\Gamma_k^{n-1}$ and $\triangle\Gamma_k^n$, respectively. Substitute (26) into (25), the derivative of the EIT measurement with respect to the two dimensional vertex displacement is

$$\begin{aligned}\frac{\partial U^{\mathbf{I},\mathbf{M}}}{\partial \mathbf{r}} &= \frac{\sin(\alpha)}{4}|\triangle\Gamma_k^{n-1}|(\sigma_0-\sigma_k)\int_{-1}^{1}(1+t)\left(\kappa_k q^{\mathbf{I}}q^{\mathbf{M}} + \nabla_{\|}u^{\mathbf{I}}\nabla_{\|}u^{\mathbf{M}}\right)|_{\triangle\Gamma_k^{n-1}}\mathrm{d}t \\ &+ \frac{\sin(\beta)}{4}|\triangle\Gamma_k^{n}|(\sigma_0-\sigma_k)\int_{-1}^{1}(1-t)\left(\kappa_k q^{\mathbf{I}}q^{\mathbf{M}} + \nabla_{\|}u^{\mathbf{I}}\nabla_{\|}u^{\mathbf{M}}\right)|_{\triangle\Gamma_k^{n}}\mathrm{d}t. \end{aligned} \tag{27}$$

In three dimensional inclusion reconstructions, the boundary of the target inclusion is usually divided into a finite number of small triangles. As it is shown in Figure 3(b), the displacement of a geometric vertex $\mathbf{v}_{e(1)}$ will affect the triangle elements $\triangle\Gamma_k^e$, for $e = 1, 2, \ldots, p$, attached with this vertex. Here, the subscript in $\mathbf{v}_{e(1)}$ is the local index of the target vertex in the triangle element $\triangle\Gamma^e$. The boundary deformation caused by the vertex displacement $\mathbf{r} = \mathbf{v}_{e(1)} - \mathbf{v}'_{e(1)}$ satisfies

$$h(L_1, L_2) = L_1 r\sin(\phi_e), \tag{28}$$

where $L_1, L_2 \in [0, 1]$ are the local coordinates at $\triangle\Gamma_k^e$, and ϕ_e is the angle between $\mathbf{r}$ and $\triangle\Gamma_k^e$. Substituting (28) into (25), the derivative of the EIT measurement with respect to the three dimensional vertex displacement is

$$\frac{\partial U^{\mathbf{I},\mathbf{M}}}{\partial \mathbf{r}} = 2\sum_{e=1}^{p}|\triangle\Gamma_k^e|\int\int_{\triangle\Gamma_k^e} L_1\left(\kappa_k q^{\mathbf{I}}q^{\mathbf{M}} + \nabla_{\|}u^{\mathbf{I}}\nabla_{\|}u^{\mathbf{M}}\right)\mathrm{d}L_1\mathrm{d}L_2. \tag{29}$$

3.3. *Conductivity sensitivity calculation*

Let the inclusion conductivity σ_k undergos a small perturbation $\delta\sigma_k$. According to the description in appendix, the EIT measurement change δU caused by the conductivity perturbation $\delta\sigma_k$ can be calculated with the volume integral (40). Since BEM only evaluates the field variables at the boundary, a BIE is derived from Gauss divergence theorem

$$\frac{\partial U^{\mathbf{I},\mathbf{M}}}{\partial \sigma_k} = -\int_{D_k} \nabla u^{\mathbf{I}} \cdot \nabla u^{\mathbf{M}} \mathrm{d}V = \frac{1}{\sigma_k}\int_{\Gamma_k} u^{\mathbf{I}} q^{\mathbf{M}} \mathrm{d}S = \frac{1}{\sigma_k}\int_{\Gamma_k} u^{\mathbf{M}} q^{\mathbf{I}} \mathrm{d}S, \qquad (30)$$

where $u = u^+$ and $q = q^+$ are electric variables at the background medium side.

4. Results and discussion

This section aims at evaluating the methods presented in the previous section. A series of numerical experiments are carried out. Firstly, the BEM solution for EIT direct problem is compared with the analytic and FEM solutions. Secondly, the proposed shape sensitivity calculation method, mentioned as SPM, is compared with the Finite Difference Method (FDM). Thirdly, characteristics of EIT shape sensitivity field are discussed. Finally, two and three dimensional inclusions are reconstructed by using the proposed shape reconstruction method.

4.1. *BEM solution for EIT direct problem*

In this example, the observation domain is a unit disk with unit conductivity. A round inclusion with 0.5 radius and 1.1 conductivity is placed at the centered of the domain. Sixteen electrodes with 0.196 width are equally spaced on the boundary of the domain. Contact impedance z between the electrode and background medium is 0.001. Sheffield pattern [17] is used to collect the artificial measurements. The analytic solution is conducted by using the method described in [21]. The first-order FEM solution is conducted with the well-established EIDORS [22]. The finite element meshes are generated from the NetGen [23].

The results are shown in Figure 4. The BEM and FEM solutions are in a good agreement with the analytic solution. With the same maximum mesh size (maximum boundary element length or finite element area), BEM solution is more accurate than FEM solution. For example, with 0.004 maximum mesh size, the relative error of BEM solution (1584 boundary elements) is 0.00816%, while the relative error of first order FEM solution (417528 volume elements) is 0.0339%. Although, more accurate solutions can be obtained by using a higher order numerical method, e.g. the Galerkin BEM [24] or the p-FEM [25], or the Method of Fundamental Solutions (MFS) [26], they will not be discussed in this paper. Later, the presented BEM with constant boundary elements is proved to be good enough for the inclusion reconstruction.

4.2. *Accuracy of shape sensitivity calculation*

In this subsection, the proposed SPM is compared with FDM for calculating shape sensitivity in EIT. Geometric configuration of the observation domain is drawn in Figure 5. An inclusion with 5.0 conductivity is located at the origin. Boundary of the

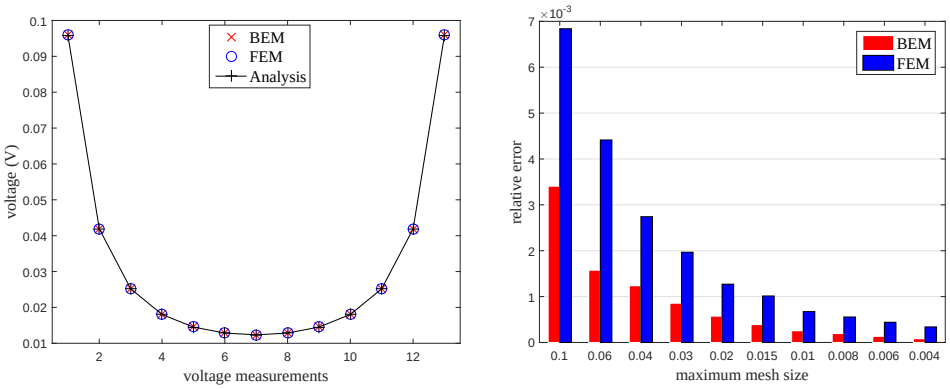

(a) (b)

Figure 4. Comparison of BEM, FEM and analytic solutions for EIT direct problem (a) first 13 measurements in Sheffield data collection pattern with 0.01 maximum mesh size, (b) relative errors of BEM and FEM solutions with different maximum mesh sizes.

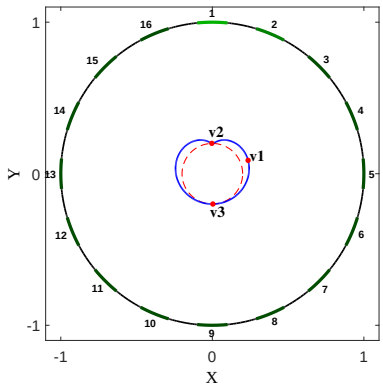

Figure 5. Geometric configuration of two dimensional domain for EIT shape sensitivity analysis.

inclusion is parameterized by Limacon function

$$\mathbf{v}(\rho,\theta) = \rho(\theta) = 0.14 \times \left(\gamma + \cos\left(\theta + \frac{\pi}{2}\right)\right), \tag{31}$$

where γ is the shape coefficient, $\mathbf{v}(\rho,\theta)$ is the vertex at the inclusion boundary, r and θ is the radius and angle variables in polar system, respectively. In Figure 5, $\gamma = 1.25$. The BEM mesh is generated with equal angle-interval $\triangle\theta$. More boundary elements are assigned to the high curvature part of the boundary. FDM solution of the shape derivative with respect to a target shape parameter α (could be a shape coefficients γ or a vertex displacement $\mathbf{r} = \mathbf{v} - \mathbf{v}'$) is evaluated by

$$J_{FMD} = \frac{\partial U}{\partial \alpha} \approx \frac{U(\alpha + \delta\alpha) - U(\alpha)}{\delta\alpha}, \tag{32}$$

where $\delta\alpha$ is small perturbation of the target parameter. We choose $\delta\alpha = 10^{-4}$ in the following tests. The red doted circle in Figure 5 is used as a reference for measuring the curvature of the inclusion boundary. Three testing points **v1**, **v2** and **v3** are placed at the different sides of the inclusion boundary.

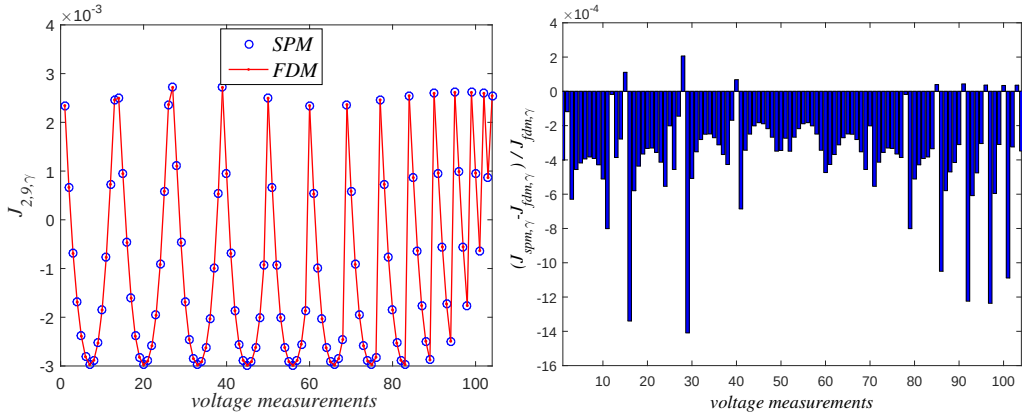

(a) (b)

Figure 6. Comparison between SPM and FEM for calculating shape sensitivity with respect to the shape coefficient γ, (a) results from SPM and FEM, (b) relative errors between these two methods.

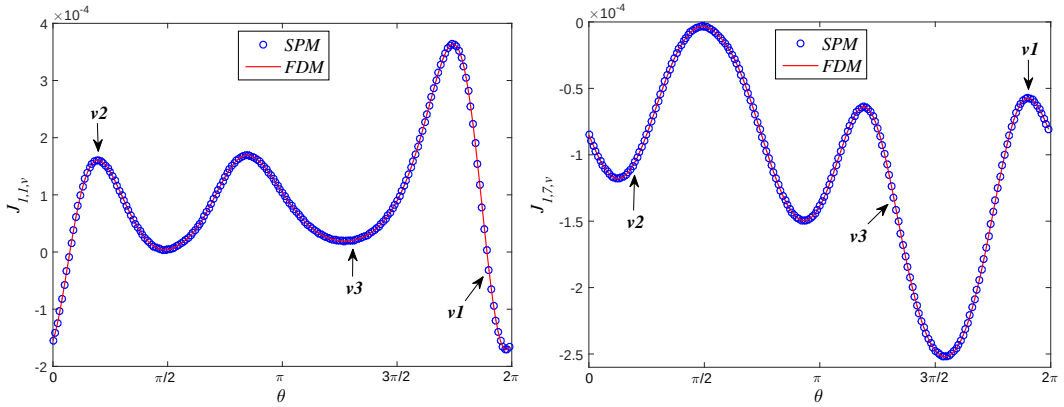

(a) (b)

Figure 7. Comparison between SPM and FEM for calculating shape sensitivity with respect to the vertex displacements, (a) shape sensitivities of $U^{1,1}$, (b) shape sensitivities of $U^{1,7}$.

In the first group of tests, the sensitivity of EIT measurements with respect to the shape coefficient changes is calculated. The results are shown in Figure 6. The $J_{i,j,\gamma} = \partial U^{i,j}/\partial\gamma$ is the sensitivity with respect to the shape coefficient γ. The $U^{i,j}$ is the j-th voltage measurement from i-th current driving pattern in Sheffield protocol. The SPM solution is evaluated by applying (31) on (25). The FDM solution is evaluated by applying $\alpha = \gamma$ on (32). The results from these two methods are quite similar. The relative error, defined as $||J_{SPM} - J_{FDM}||/||J_{FDM}||$, is less than 0.15%.

In the second group of tests, the deformation of the inclusion boundary is caused by the vertex displacement in BEM mesh. The vertex displacement is on the normal direction of the boundary. The results are shown in Figure 7. The $J_{i,j,v}(\theta) = \partial U^{i,j}/\partial\mathbf{r}$ is the sensitivity of $U^{i,j}$ with respect to the vertex displacement $\mathbf{r}(\theta) = (\mathbf{v}(\theta) - \mathbf{v}'(\theta))$ at the boundary normal direction. The SPM solution is evaluated by (27). The FDM solution is evaluated by applying $\alpha = \mathbf{r}$ on (32). The results from these two methods are quite similar. The relative error is less than 0.1%.

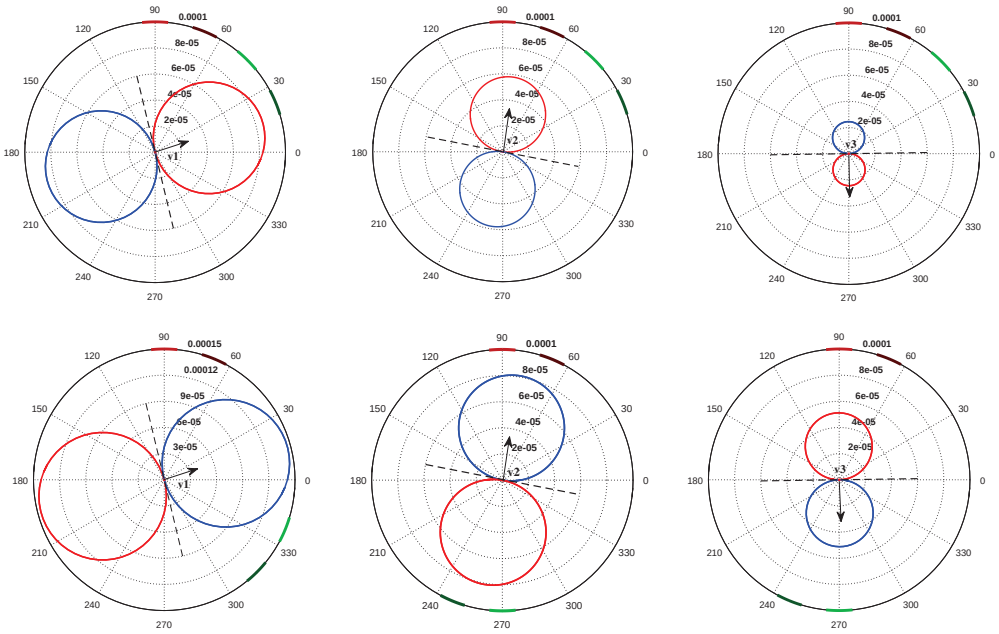

Figure 8. Shape sensitivity with respect to unit displacements of testing points **v1**, **v2** and **v3** on different moving directions.

4.3. *Analysis of shape sensitivity field*

In this subsection, the characteristics of EIT shape sensitivity field are discussed. The inclusion boundary is discretized with equal arc-length-interval. Lengths of the boundary elements are nearly the same. As a result, displacement of different vertices leads to nearly the same amount of boundary deformation.

In the first group of tests, the shape sensitivity $J_{i,j,v} = \partial U^{i,j}/\partial \mathbf{r}$ is calculated at the testing points **v1**, **v2** and **v3**, where $U^{i,j}$ is the EIT measurement, and $\mathbf{r}$ is the displacement of the testing point. Figure 8 shows the results. The illustrations are presented in polar coordinates system. The vertex displacement $\mathbf{r}$ is on all the possible directions $[0, 2\pi]$. The angle indicates the vertex displacement direction. The dotted and arrow lines denote the tangent and normal directions of the inclusion boundary at a certain testing point. The radius indicates the absolute value of shape sensitivity. The red and blue solid circles are the shape sensitivities caused by the positive and negative displacements, respectively. The driven electrodes, at the peripheral of the observation domain, are painted in red, while the measurement electrodes are painted in green. The red and blue circles are strict symmetric along the dotted line. This implies that the positive and negative vertex displacements lead to the same amount of measurement changes. On the other hand, the shape sensitivity achieves the maximum at the boundary normal direction, and is zero at the boundary tangent directions. This states that only the boundary displacement in the normal direction leads to measurement changes. The boundary displacement in the tangential direction does not contribute to shape deformations (at least in the first order formation). They only re-parameterize the existing boundaries.

The conductivity contrast $\kappa = \sigma_1/\sigma_0$ between the inclusion and background medium will influence the shape sensitivity. Figure 9 shows the evaluation of $J_{norm}(v) = \|J_{i,j,v}\|$ with respect to κ. The shape sensitivity is calculated at the boundary normal direction.

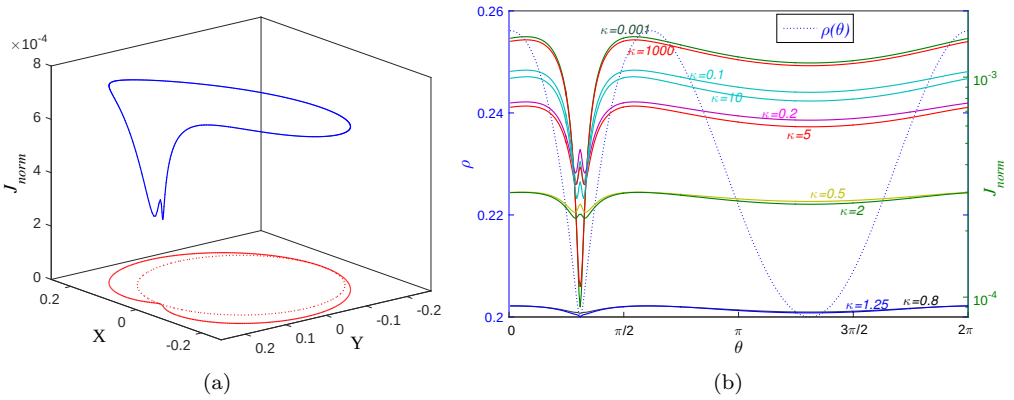

Figure 9. Shape sensitivity of the inclusion boundary for different conductivity, (a) shape sensitivity with $\kappa = \sigma_1/\sigma_0 = 0.8$, (b) shape sensitivity with different κ.

The dotted line is used to illustrate the shape of the inclusion boundary. The shape sensitivity can be enhanced by increasing the conductivity contrast, which implies that the shape-based method will be more efficient for reconstructing the inclusions with high conductivity contrast, $\kappa \gg 1$ or $\kappa \ll 1$. However, the sensitivity enhancement is more and more insignificant with κ approaching zero or infinity, which implies a limited spatial resolution of inclusion boundary reconstruction. Moreover, the shape sensitivity at the convex boundary part is larger than that at the concave boundary part. The phenomenon exists in both $\kappa > 1$ and $\kappa < 1$ cases, and is more obvious in enhanced conductivity contrast cases ($\kappa \gg 1$ or $\kappa \ll 1$). This characteristic of the shape sensitivity field may serve for EIT image analysis, e.g. assigning confidences for different parts of boundary.

Another factor influencing the shape sensitivity field is the location of the target inclusion. The shape sensitivity mappings are calculated with seven different inclusion locations, as shown in Figure 10. The results show that the measurements are more sensitive to the shape deformations near the electrodes and less sensitive to the shape deformations far from the electrodes. The results are easy to be understand since the EIT measurements are only collected at the outermost boundary of observation domain, that leads to a weak electrical field at the observation field away from the driving and measuring electrodes.

4.4. *Two dimensional inclusion reconstruction with known conductivity*

In this subsection, two dimensional inclusions are reconstructed by using the presented shape-based method. The target boundary is a simplification of human chest, as shown in Figure 11. The heart shaped inclusion is with 5.0 conductivity. Its boundary is controlled by the Limacon function (31). The lung shaped inclusions have 0.1 conductivity. Their boundaries are controlled by three-order Fourier function [20]. Residual between the estimated and measured EIT data, denoted with $Res = \|U - U^*\|$, is used to evaluate the accuracy of the reconstruction result. Mismatch between the target and reconstructed boundaries is measured by the Hausdorff distance

$$Hd(\Gamma_{rec}, \Gamma_{target}) = \frac{1}{R} \max \min \|\mathbf{v}_{rec} - \mathbf{v}_{target}\|, \tag{33}$$

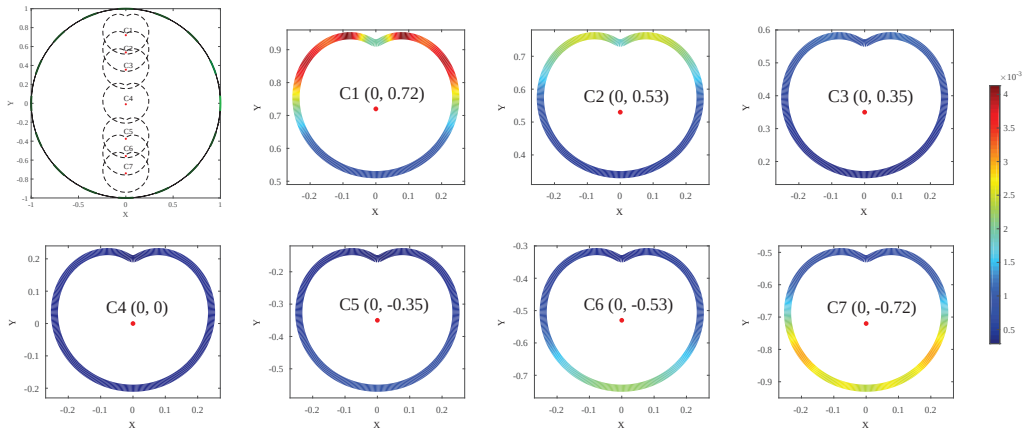

Figure 10. Evolution of shape sensitivity with respect to inclusion location.

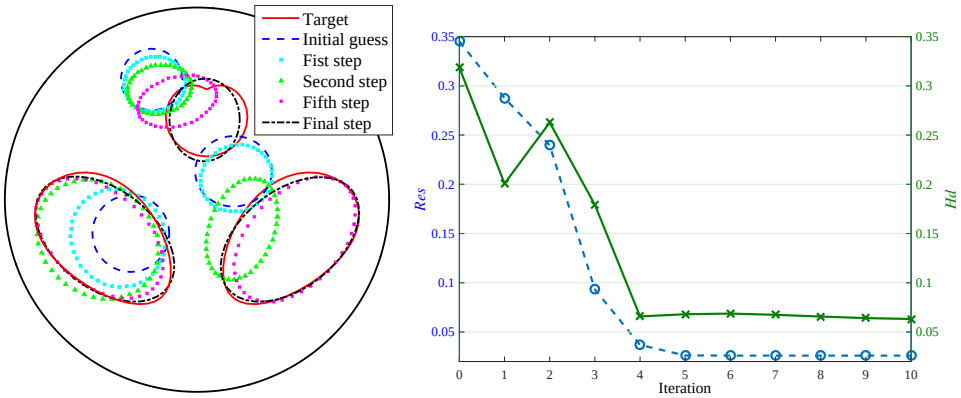

(a) (b)

Figure 11. Two dimensional inclusion boundary reconstruction with 3% Gaussian noise, (a) estimated and target boundaries, (b) evolution of Residual (Res) and Hausdroff distance (Hd) with respect to iteration.

where R is the radius of the observation domain, $\mathbf{v}_{rec}$ and $\mathbf{v}_{target}$ are the points at the reconstructed and target boundaries, respectively. To avoid an inverse crime, BEM mesh consisting of 960 boundary elements is used to calculate the artificial measured data $U^* = U(\Gamma_{target})$, and the BEM mesh consisting of 320 boundary elements is used to evaluate the simulated data $U(\Gamma_{rec})$. The conductivity of the inclusions is known. The initial guesses of the inclusion boundary are three circles randomly placed in the observation domain. The measurements are contaminated by 3% Gaussian noise. As shown in Figure 11, after starting from the initial guess, the estimated boundary tends to the targets in a fast and stable way. After eight iterations, the residual Res is smaller than 0.02, and the Hausdroff distance Hd is under 0.27.

To further test the boundary reconstruction performance, the artificial EIT measurements are contaminated by noise over the range of 1% to 10%. One hundred tests are conducted for each noise level. The initial boundary guesses are still circles, but with random locations. The Newton-type iteration stops at $|Res^k - Res^{k-1}|/Res^{k-1} < 10^{-5}$, where Res^k is the residual in k-th iteration, and $n = k$ is the number of iterations needed to achieve convergence. Some of the results are shown in Figure 12. Statistical analysis of the results is tabulated in Table 1. The averages of the quantitative indexes,

Table 1. Quantitative analysis of inclusion boundary reconstruction results with different levels of noise.

Noise level	Res_{avg}	Res_{std}	Hd_{avg}	Hd_{std}	n_{avg}	r_{fail}
1%	0.018	$6.8e^{-4}$	0.040	0.017	10	0.11
3%	0.025	$7.1e^{-3}$	0.044	0.033	10	0.11
5%	0.035	$1.3e^{-2}$	0.059	0.065	10	0.14
10%	0.064	$1.6e^{-2}$	0.087	0.122	10	0.18

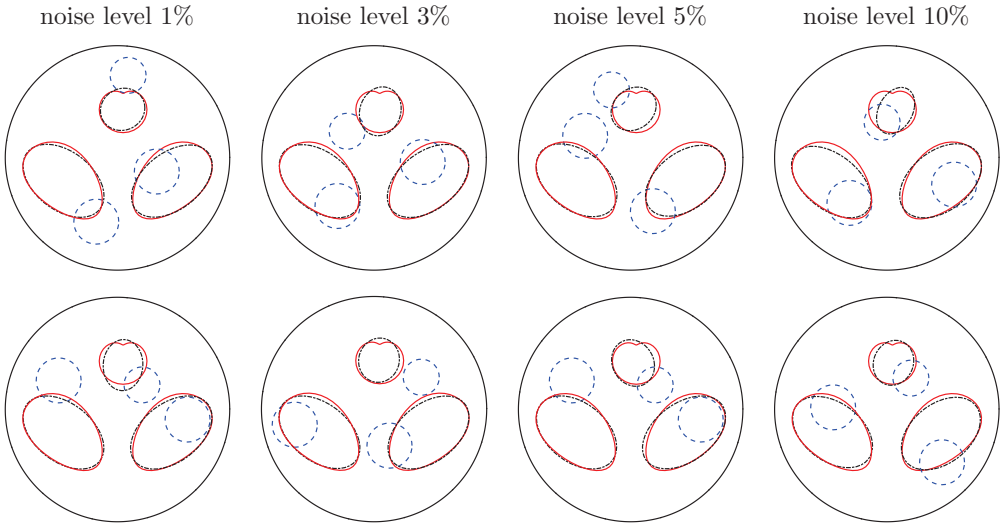

Figure 12. Two dimensional inclusion boundary reconstruction with randomly selected initial boundary guesses and different levels of noise.

denoted with Res_{avg} and Hd_{avg}, are used to evaluate the reconstruction accuracy. The standard deviations of the quantitative indexes, denoted with Res_{std} and Hd_{std}, are used to evaluate the reconstruction stability. The noise will reduce the accuracy and stability of the boundary reconstruction. However, the results are still acceptable even in the case with 10% noise. The mismatch of the reconstructed and exact boundaries is mainly caused by the concave boundary part, whose shape sensitivity is comparatively small. In most of the tests, ten iterations are enough to achieve convergence.

As described in the previous section, the Newton-type boundary estimation does not always achieve the global minimization. Here, the fail ratio r_{fail} is used to represent the possibility of the unsuccessful reconstruction. The unsuccessful reconstruction includes the inclusions exceeding the observation domain or the inclusions overlapped with each other. As it is shown in Table 1, the measurement noise slightly influences the fail ratio. The fail ratio is 0.19 in the tests with 10% noise, comparing with 0.11 fail ratio in the tests with 3% noise. The main factor influencing the fail ratio is the initial guesses. In the tests with poor initial guesses, the boundary reconstruction has a big chance to fail. The poor initial guesses are the ones significantly different from the exact, e.g. misplacing the heart shaped inclusion at the lung shaped inclusion.

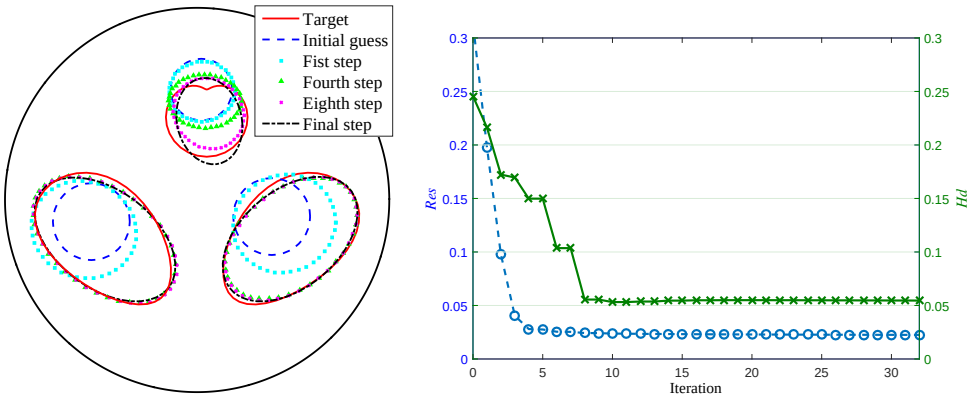

(a) (b)

Figure 13. Two dimensional inclusion boundary and conductivity simultaneous reconstruction with 3% Gaussian noise, (a) estimated and target boundaries, (b) evolution of Residual (Res) and Hausdroff distance (Hd) with respect to iteration.

4.5. *Two dimensional inclusion reconstruction with unknown conductivity*

In this subsection, the conductivity of the inclusions is unknown. As a result, the boundary and conductivity of the inclusions are simultaneously reconstructed from the EIT measurements. The iteration starts from four steps of boundary reconstruction. Then the conductivity and boundary reconstruction will conduct alternately. The results are shown in Figure 13. The EIT measurements are with 3% Gaussian noise. The mean absolute error of the guessed (reconstructed) conductivity is denoted with Er. The inclusion boundary and conductivity simultaneous reconstruction is more difficult. The first few of iterations are mainly focused on the reconstruction of the boundary of inclusions. Ten iterations are enough to reconstruct the boundary of inclusions with good accuracy, $Hd < 0.06$. After that, more iterations are conducted to improve the boundary reconstruction result and achieve good conductivity estimation. The final Er is 0.140, comparing with 0.239 initial Er.

To test the influences of the initial conductivity guesses on the final inclusion reconstruction results, a series of tests are conduced. The initial conductivity values are randomly selected. The initial conductivity error is denoted with Init. Er, and is over the range of 0 to 40%. One hundred tests are conducted for each level of Init. Er. The reconstruction results are shown in Figure 14. Statistical analysis of the results is tabulated in Table 2. The boundary reconstruction is quite robust to the initial conductivity guesses. The Res and Hd are quite similar in the tests with different levels of Init. Er. However, incorrect initial conductivity guesses will increase the possibility of unsuccessful reconstruction. The algorithm has a big chance (more than 15%) to fail when Init. Er is more than 20%. Furthermore, incorrect initial conductivity guesses will also increase the number of iterations needed for convergence.

4.6. *Three dimensional inclusion reconstruction*

In 3D case, the observation domain is a simplified human chest model, as shown in Figure 15. The surfaces of the target inclusions are parameterized by four order spherical harmonics [27]. Each surface is controlled by 27 shape coefficients γ, and there are 81 shape coefficients in total. The heart (painted in red) is with 5.0 conductivity,

Table 2. Quantitative analysis of inclusion reconstruction results with different initial conductivity guesses.

Init. Er	Res_{avg}	Res_{std}	Hd_{avg}	Hd_{std}	Er_{avg}	Er_{std}	n_{stop}	$ratio_{fail}$
0% -10%	0.025	$2.5e^{-3}$	0.050	0.030	0.043	0.017	10	0.07
10%-20%	0.024	$1.6e^{-3}$	0.046	0.022	0.096	0.030	21	0.06
20%-30%	0.024	$1.7e^{-3}$	0.046	0.025	0.133	0.032	32	0.15
30%-40%	0.024	$1.6e^{-3}$	0.047	0.028	0.149	0.042	40	0.30

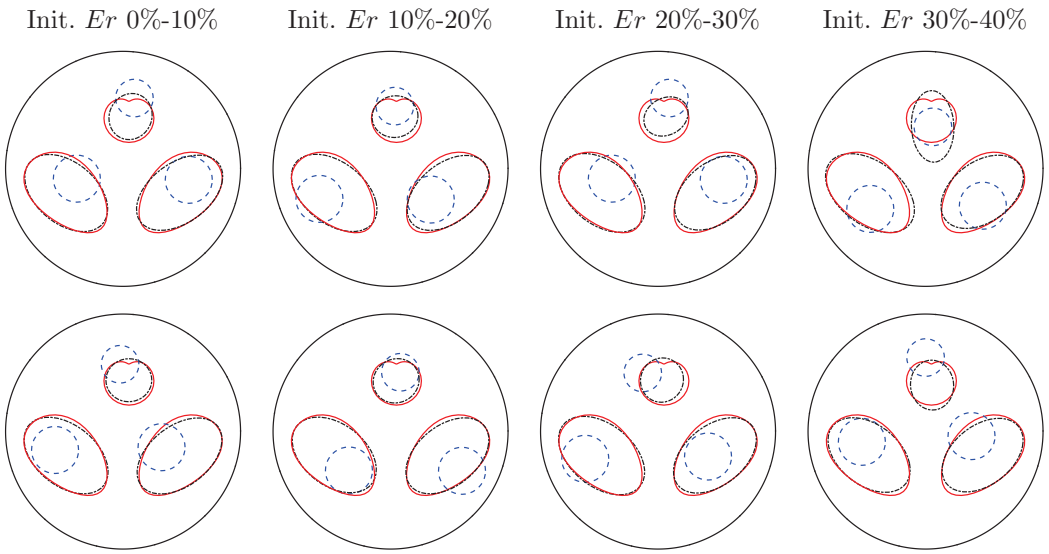

Figure 14. Two dimensional inclusion boundary and conductivity simultaneous reconstruction with 3% Gaussian noise and randomly selected initial guesses.

while the lungs (painted in green) are with 0.1 conductivity. Four layers of electrodes are fixed at the peripheral of tank. The tank is 0.25 radius and 0.5 height. The EIT measurements are collected from Sheffield protocol. The measurements are with 1% Gaussian random noise. The shape sensitivity with respect to the shape coefficients γ is calculated by SPM and FDM. The results are shown in Figure 16. The results from these two methods are quite similar. The means of absolute differences between the results from SPM and FDM are smaller than 0.03.

The reconstruction results are shown in Figure 17. After starting from the initial guesses, the estimated surfaces tend to the targets step by step. After seven iterations, the recovered inclusions are quite similar with the targets. The residual Res is smaller than 0.01. The Hausdroff distances Hd of the heart, left lung and right lung shaped inclusions are 0.086, 0.030 and 0.028, respectively. To show the detail of the 3D boundary reconstruction, the exact inclusions are fitted by three ellipsoids. The geometric centers and the semi-principal axes of the ellipsoids are used to build the local coordinate system, as shown in Figure 17. The orthogonal 2D profiles of the 3D inclusions are drawn in the local coordinate systems, as shown in Figure 18. Reconstruction of the left and right lung shaped inclusions are more accurate than the reconstruction of the heart shaped inclusion. The presented shape-based inclusion reconstruction method is good at recovering big size inclusions with convex boundary. The small size inclusion with concave boundary is hard to be recovered.

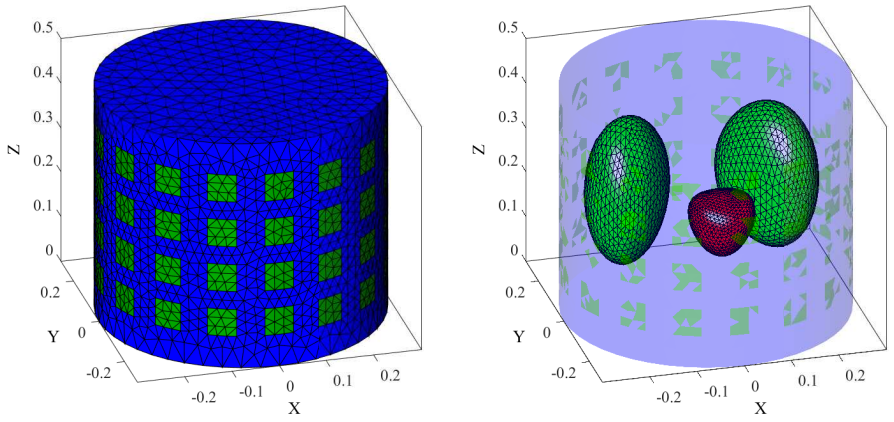

Figure 15. Geometric configuration of observation domain for three dimensional inclusion reconstruction, (a) observed tank and electrodes, (b) target inclusions.

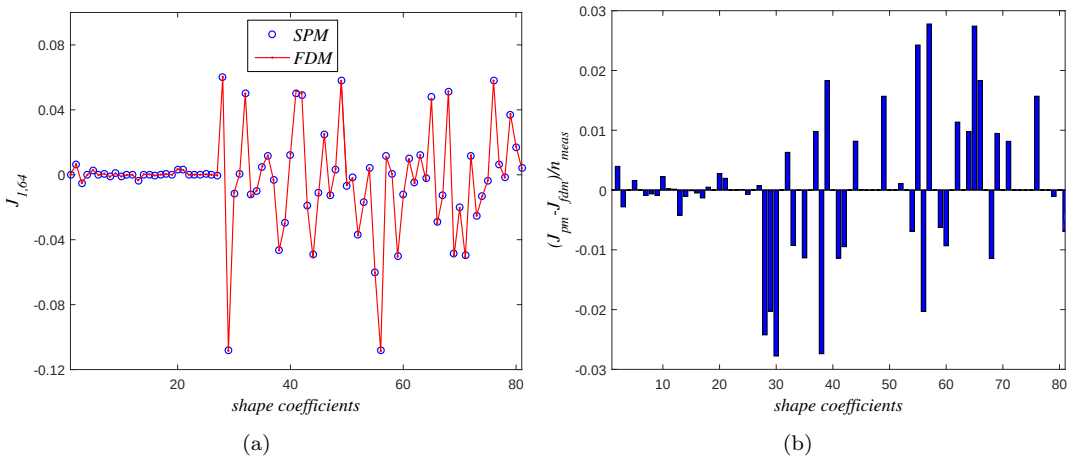

Figure 16. Shape sensitivities calculation from SPM and FDM in three dimensions, (a) shape sensitivity of $U^{1,64}$, (b) average errors between SPM and FDM with different shape coefficients.

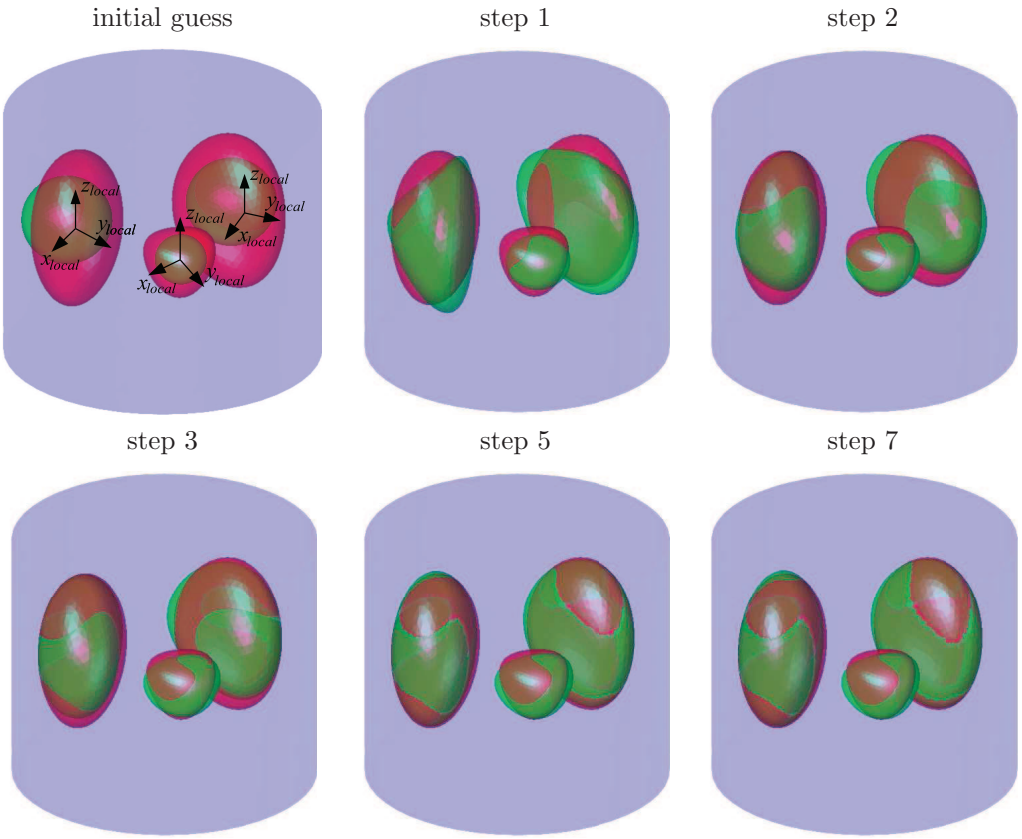

Figure 17. Three dimensional inclusion boundary reconstruction for simplified human chest model.

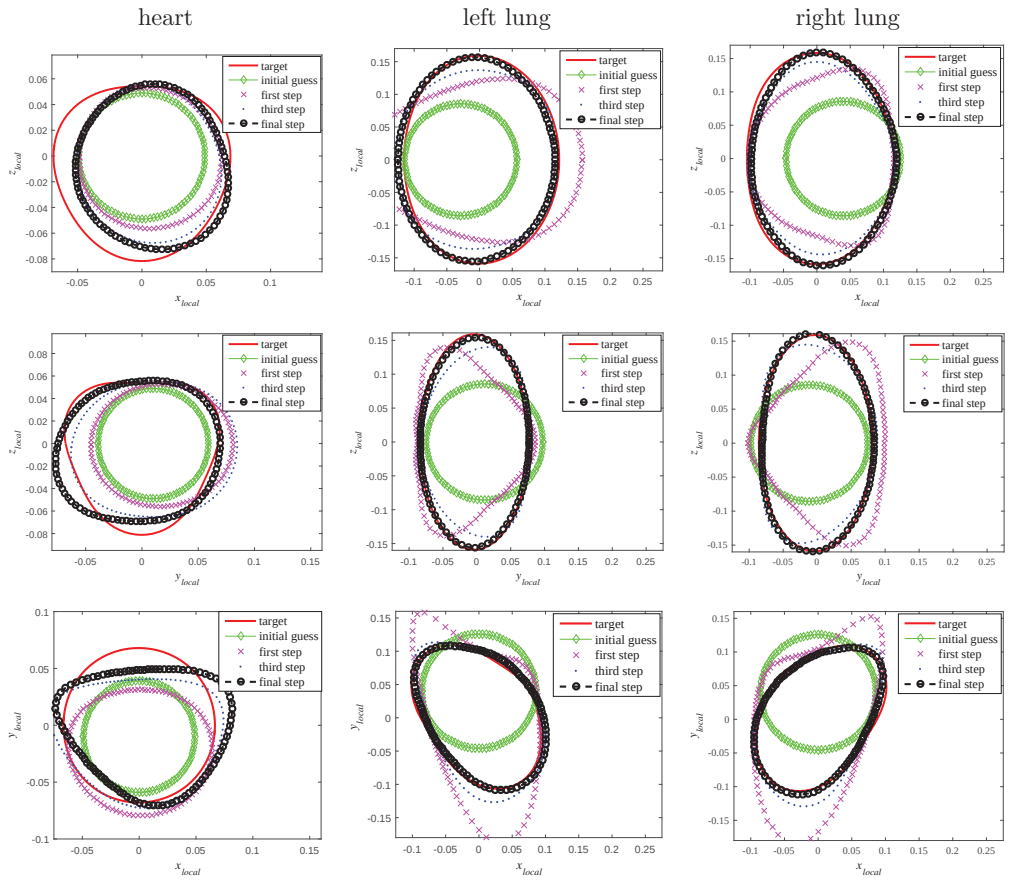

Figure 18. Two dimensional profiles of three dimensional inclusions reconstruction.

5. Conclusion

A shape-based inclusion reconstruction method and its numerical implementation were presented. A boundary integral formula was derived for calculating the shape sensitivity in EIT. Some characteristics of EIT shape sensitivity field were discussed. Firstly, the EIT measurements were more sensitive to the boundary deformations at the convert boundary part or at the regions near the sensing electrodes. Secondly, the enhanced conductivity contrast between the inclusion and background medium could improve the shape sensitivity, but the improvement is limited. According to the numerical results, the proposed methods performed well for both 2D and 3D inclusion reconstructions. The estimated inclusion boundary was well matched with the exact boundary (the Hausdroff distance was less than 10% radius of the observation domain), and the estimated inclusion conductivity was with less than 15% relative error.

However, due to ill-posedness of EIT inverse problem, the inclusion boundary reconstruction has a possibility to be non-convergent (unstable). The measurement noise has a slight influence on the stability of reconstruction, while a good initial guess can significantly improve the stability. Although this can be remitted by improving the accuracy of the initial boundary and conductivity guesses, our future focus is still on on the development of the high robust implementation of the proposed method and its application on real data.

Acknowledgements

We would like to thank the editors and the referees for their carefully reviewing and valuable comments, which helped us to improve the manuscript.

Funding

The authors appreciate the support from the National Natural Science Foundation of China (No. 61401304, No. 61571321) and the Science and Technology Innovation Plan of Tianjin (No. 16PTSYJC00060).

References

[1] Zou Y, Guo Z. A review of electrical impedance techniques for breast cancer detection. Medical Engineering and Physics. 2003;25(2):79-90.

[2] Pak DD, Rozhkova NI, Kireeva MN, Ermoshchenkova MV, Nazarov AA, Fomin DK, Rubtsova NA. Diagnosis of breast cancer using electrical impedance tomography. Biomedical Engineering. 2012;46(4):154-157.

[3] Frerichs I. A review of electrical impedance techniques for breast cancer detection. Physiological Measurement. 2000;21(2):R1-R21.

[4] Bikker IG, Leonhardt S, Bakker J, Gommers D. Lung volume calculated from electrical impedance tomography in ICU patients at different PEEP levels. Intensive Care Medicine. 2009;35(8):1362-1367.

[5] Dong F, Jiang ZX, Qiao XT, Xu LA. Application of electrical resistance tomography to two-phase pipe flow parameters measurement. Flow Measurement and Instrumentation. 2003;14(4):183-192.

[6] Ismail I, Gamio JC, Bukhari SA, Yang WQ. Tomography for multi-phase flow measurement in the oil industry. Flow Measurement and Instrumentation. 2005;16(2):145-155.
[7] Haddar H, Kress R. A conformal mapping method in inverse obstacle scattering. Complex Variables and Elliptic Equations. 2014;59(6):863-882.
[8] Cakoni F, Kress R. Integral equation methods for the inverse obstacle problem with generalized impedance boundary condition. Inverse Problems. 2012;29(1):015005-015027.
[9] Soleimani M, Lionheart WRB, Dorn O. Level set reconstruction of conductivity and permittivity from boundary electrical measurements using experimental data. Inverse Problems in Science and Engineering. 2006;14(2):193-210.
[10] Dyhoum TE, Aykroyd RG, Lesnic D. Reconstructing rigid inclusions in the complete-electrode model of ERT, In: Inverse Problems and Computational Mechanics, Volume 2, (eds. L. Marin, L. Munteanu and V. Chiroiu), The Publishing House of the Romanian Academy, Bucharest, Romania, Chapter 4, pp.73-102.
[11] Somersalo E, Cheney M, Isaacson D. Existence and uniqueness for electrode models for electric current computed tomography. SIAM Journal on Applied Mathematics. 1992;52(4):1023-1040.
[12] Duraiswami R, Chahine GL, Sarkar K. Boundary element techniques for efficient 2-D and 3-D electrical impedance tomography. Chemical Engineering Science. 1997;52(13):2185-2196.
[13] Babaeizadeh S, Brooks DH. Electrical impedance tomography for piecewise constant domains using boundary element shape-based inverse solutions. IEEE Transactions on Medical Imaging. 2007;26(5):637-647.
[14] Xu YY, Dong F, Tan C. Electrical resistance tomography for locating inclusions using analytical boundary element integrals and their partial derivatives. Engineering Analysis with Boundary Elements. 2010;34(10):876-883.
[15] Tan C, Xu YY, Dong F. Determining the boundary of inclusions with known conductivities using a LevenbergCMarquardt algorithm by electrical resistance tomography. Measurement Science and Technology. 2011;22(10):104005-104017.
[16] Ren SJ, Dong F, Xu YY, Tan C. Reconstruction of the three-dimensional inclusion shapes using electrical capacitance tomography. Measurement Science and Technology. 2014;25(2):025403-025418.
[17] Brown BH, Seagar AD. The Sheffield data collection system. Clinical Physics and Physiological Measurement. 1987;8(4A):91-97.
[18] Afraites L, Dambrine M, Kateb D. On second order shape optimization methods for electrical impedance tomography. SIAM Journal on Control and Optimization. 2008;47(3):1556-1590.
[19] Brebbia CA, Telles JCF, Wrobel LC. Boundary element techniques: theory and applications. New York (NY): Springer-Verlag; 1984.
[20] Han DK, Prosperetti A. A shape decomposition technique in electrical impedance tomography. Journal of Computational Physics. 1999;155(1):75-95.
[21] Winkler R, Rieder A. Resolution-controlled conductivity discretization in electrical impedance tomography. SIAM Journal on Imaging Sciences. 2014;7(4):2048-2077.
[22] Adler A, Lionheart WR. Uses and abuses of EIDORS: an extensible software base for EIT. Physiological Measurement. 2006;27(5):S25-S42.
[23] Schöberl J. NETGEN An advancing front 2D/3D-mesh generator based on abstract rules. Computing and Visualization in Science. 1997;1(1):41-52.
[24] Xu Y, Dong F. Galerkin boundary element method for the forward problem of ERT. Flow Measurement and Instrumentation. 2010;21(3):172-177.
[25] Crabb MG. Convergence study of 2D forward problem of electrical impedance tomography with high-order finite elements. Inverse Problems in Science and Engineering. 2017; in printting, published online.
[26] Dyhoum TE, Lesnic D, Aykroyd RG. Solving the complete-electrode direct model of ERT using the boundary element method and the method of fundamental solutions. Electronic Journal of Boundary Elements. 2014;12(3):26-71.

[27] Zacharopoulos AD, Arridge SR, Dorn O, Kolehmainen V, Sikora J. Three-dimensional reconstruction of shape and piecewise constant region values for optical tomography using spherical harmonic parametrization and a boundary element method. Inverse Problems. 2006;22(5):1509-1532.
[28] Aghasi A, Miller EL. Sensitivity calculations for Poisson's equation via the adjoint field method. IEEE Geoscience and Remote Sensing Letters. 2012;9(2):237-241.
[29] Polydorides N, Lionheart WR. A Matlab toolkit for three-dimensional electrical impedance tomography: a contribution to the Electrical Impedance and Diffuse Optical Reconstruction Software project. Measurement Science and Technology. 2002;13(12):1871-1883.

6. Appendices

In this section, the calculation formula of the sensitivity of the EIT measurement with respect to the conductivity perturbation is derived. The starting point is the reciprocal property of electric field. For a given data collection pattern $\{\mathbf{I}, \mathbf{M}\}$, its reciprocal pattern is defined as $\{\mathbf{M}, \mathbf{I}\}$ in which the current supply and voltage collection terminals were interchanged. The electric potentials evaluated with $\{\mathbf{M}, \mathbf{I}\}$ and $\{\mathbf{I}, \mathbf{M}\}$ are denoted with $u^{\mathbf{I}}$ and $u^{\mathbf{M}}$, respectively.

According to Green's first identity and complete electrode condition (2), the integral equation for the scalar field $u^{\mathbf{I}}$ and the vector field $\nabla u^{\mathbf{M}}$ is given by

$$\sum_{l=1}^{L} \int_{E_l} u^{\mathbf{I}} \sigma^{\mathbf{M}} q^{\mathbf{M}} \mathrm{d}S = \int_{\Omega} \sigma^{\mathbf{M}} \nabla u^{\mathbf{I}} \cdot \nabla u^{\mathbf{M}} \mathrm{d}V, \tag{34}$$

where $q^{\mathbf{M}} = \nabla u^{\mathbf{M}} \cdot \nu$, and $\sigma^{\mathbf{M}}$ is the conductivity distribution associated with the current pattern $\mathbf{M}$.

Similarly, the integral equation for the scalar field $u^{\mathbf{M}}$ and the vector field $\nabla u^{\mathbf{I}}$ is

$$\sum_{l=1}^{L} \int_{E_l} u^{\mathbf{M}} \sigma^{\mathbf{I}} q^{\mathbf{I}} \mathrm{d}S = \int_{\Omega} \sigma^{\mathbf{I}} \nabla u^{\mathbf{M}} \cdot \nabla u^{\mathbf{I}} \mathrm{d}V, \tag{35}$$

where $q^{\mathbf{I}} = \nabla u^{\mathbf{I}} \cdot \nu$, and $\sigma^{\mathbf{I}}$ is the conductivity distribution associated with the current pattern $\mathbf{I}$.

Subtracting (35) from (34) results

$$\sum_{l=1}^{L} \int_{E_l} u^{\mathbf{I}} \sigma^{\mathbf{M}} q^{\mathbf{M}} \mathrm{d}S - \sum_{l=1}^{L} \int_{E_l} u^{\mathbf{M}} \sigma^{\mathbf{I}} q^{\mathbf{I}} \mathrm{d}S = \int_{\Omega} \left(\sigma^{\mathbf{M}} - \sigma^{\mathbf{I}}\right) \nabla u^{\mathbf{I}} \cdot \nabla u^{\mathbf{M}} \mathrm{d}V. \tag{36}$$

According to the boundary condition (2), the boundary integral terms in (36) satisfy

$$\begin{aligned} &\int_{E_l} u^{\mathbf{M}} \sigma^{\mathbf{I}} q^{\mathbf{I}} \mathrm{d}S = \int_{E_l} \left(V_l^{\mathbf{M}} - z_l \sigma^{\mathbf{M}} q^{\mathbf{M}}\right) \sigma^{\mathbf{I}} q^{\mathbf{I}} \mathrm{d}S \\ &= V_l^{\mathbf{M}} I_l - \int_{E_l} \left(V_l^{\mathbf{I}} - u^{\mathbf{I}}\right) \sigma^{\mathbf{M}} q^{\mathbf{M}} \mathrm{d}S = V_l^{\mathbf{M}} I_l - V_l^{\mathbf{I}} M_l + \int_{E_l} u^{\mathbf{I}} \sigma^{\mathbf{M}} q^{\mathbf{M}} \mathrm{d}S, \end{aligned} \tag{37}$$

where $V_l^{\mathbf{I}}$ and $V_l^{\mathbf{M}}$ are the voltage responds to $\{\mathbf{I}, \mathbf{M}\}$ and $\{\mathbf{M}, \mathbf{I}\}$, respectively.

Substituting (37) into (36), the EIT measurements from a pair of reciprocal data collection patterns are related by

$$-\int_{\Omega}\left(\sigma^{\mathbf{I}}-\sigma^{\mathbf{M}}\right)\nabla u^{\mathbf{I}}\cdot\nabla u^{\mathbf{M}}\mathrm{d}V=\mathbf{I}^{T}\mathbf{V}^{\mathbf{M}}-\mathbf{M}^{T}\mathbf{V}^{\mathbf{I}}=U^{\mathbf{I},\mathbf{M}}\left(\sigma^{\mathbf{I}}\right)-U^{\mathbf{M},\mathbf{I}}\left(\sigma^{\mathbf{M}}\right), \quad (38)$$

where $U(\sigma)$ is used to emphasize the dependence of the measurement on the conductivity distribution. When $\sigma^{\mathbf{I}}=\sigma^{\mathbf{M}}=\sigma$, the conductivity at entire observation domain keeps the same during $\mathbf{I}$ and $\mathbf{M}$, and $U^{\mathbf{I},\mathbf{M}}(\sigma)=U^{\mathbf{M},\mathbf{I}}(\sigma)$ because the volume integral on the above equation equals to zero. This means that the relationship between an driving electric current density and the resulting electric potential is unchanged if the current applying terminals and the voltage measuring terminals are interchanged. This reciprocal property is helpful for avoiding redundant measurements. For example, only half of the Sheffield measurements is independent.

On the other hand, the unequal conductivity $\sigma^{\mathbf{M}}=\sigma^{\mathbf{I}}+\delta\sigma$, with $\delta\sigma\neq 0$, leads to the following conductivity sensitivity formula:

$$\begin{aligned}\delta U^{\mathbf{I},\mathbf{M}} &= U^{\mathbf{I},\mathbf{M}}\left(\sigma+\delta\sigma\right)-U^{\mathbf{I},\mathbf{M}}\left(\sigma\right)=U^{\mathbf{M},\mathbf{I}}\left(\sigma+\delta\sigma\right)-U^{\mathbf{I},\mathbf{M}}\left(\sigma\right)\\ &= -\int_{\Omega}\delta\sigma\nabla u^{\mathbf{I}}\left(\sigma\right)\cdot\nabla u^{\mathbf{M}}\left(\sigma+\delta\sigma\right)\mathrm{d}V, \quad (39)\end{aligned}$$

where $\sigma=\sigma^{\mathbf{I}}$ is used to simplify the notation. Applying the approximation $u(\sigma+\delta\sigma)=u(\sigma)+\delta\sigma$ on (39) and ignoring the high order terms in the result, a widely used first-order conductivity sensitivity formula is derived

$$\delta U^{\mathbf{I},\mathbf{M}}=-\int_{\Omega}\delta\sigma\nabla u^{\mathbf{I}}\left(\sigma\right)\cdot\nabla u^{\mathbf{M}}\left(\sigma\right)\mathrm{d}V. \quad (40)$$

Although the above conductivity sensitivity formula can be derived from the other methods, such as: the adjoint field method [28] and perturbation method [29], this paper mainly focus on the derivation of the shape sensitivity formula with (39).